Application of Schwarz-Christoffel mapping to permanent-magnet linear motor analysis

Application of Schwarz-Christoffel Mapping to Permanent-Magnet Linear Motor Analysis

D. C. J. Krop, E. A. Lomonova, and A. J. A. Vandenput

Electromechanics and Power Electronics Group, Department of Electrical Engineering, Eindhoven University of Technology, 5600 MB, Eindhoven, The Netherlands

Several well-known analytical techniques exist for the force profile analysis of permanent-magnet linear synchronous motors. These techniques, however, make significant simplifications in order to obtain the magnetic field distribution in the air gap. From the field distribution, the force profile can be found. These widely used techniques provide a reasonable approximation for force profile analysis, but fail to give really accurate results in the sense of the exact shape of the force profile caused by effects that due to simplification are not fully included. To obtain the exact shape for the force profile in these cases, the computationally expensive finite-element method (FEM) is often applied. In this paper, an elegant semianalytical approach is presented to acquire the force profile. First, the magnetic field distribution in the air gap is determined by means of Schwarz-Christoffel (SC) mapping. The SC mapping allows a slotted structure of the machine to be mapped to a geometrically simpler domain for which analytic solutions are available. Subsequently, the field solution in the slotted structure can be determined by applying the mapping function to the field distribution in the simplified domain. From the resulting field distribution, the force profile is calculated by means of the Maxwell stress tensor. The results are compared with those from the commonly used equivalent magnetic circuit modeling and 2-D FEM software to demonstrate the accuracy which can be reached by application of the SC method.

***Index Terms*—Analytical model, conformal mapping, end effects, magnetic equivalent circuit, permanent-magnet linear synchronous machine, Schwarz-Christoffel mapping, slotted structure.**

I. Introduction

PERMANENT-MAGNET linear synchronous machines (PMLSMs) are utilized in applications where a high force density is required. Linear motion can be realized with "conventional" rotation motors by mechanical conversion of rotating movement into translational movement. However, when a high efficiency and high force density are required, preference is given to a PMLSM. Although rotational and translational permanent-magnet motors operate according to the same electromagnetic principles, there are major discrepancies between them that might not be directly obvious. Simply, one could state that a PMLSM is the equivalent of an unrolled rotational permanent-magnet synchronous motor. In that case, no major additional problems are to be expected. This is unfortunately not the case. The unrolling causes the geometry of the motor to lose its periodicity. This has an important influence on the magnetic field distribution near the ends of the the motor. The field distribution is now not only confined to the interior of the machine, but extended to all the space surrounding the machine. The air-gap field distribution is of prime importance for determining the force on the machine. Consequently, extra components in the force profile of the PMLSM are introduced due to this nonperiodicity and nonconfined field distribution in comparison with a rotational motor that need to be taken into account. Depending on the prerequisites of the application for which a PMLSM is to be designed, it is important during the design to get a good prediction of the force profile of the PMLSM.

A cross section with some parameters of the analyzed PMLSM is depicted in Fig. 1. More machine parameters indicated in Fig. 1 can be found in the Appendix. Many techniques are available to determine the magnetic field distribution in the air gap of such devices. All are based on Maxwell's equations. The equations, however, cannot be solved analytically for most practical geometries. Therefore, assumptions and simplification are made to obtain an approximate solution of the field distribution in the air gap. It can be shown [1] that the two three-dimensional electromagnetic curl equations of Maxwell's equations can be reduced to equivalent electric circuit equations:

$$\nabla \times \mathbf{E} = -\frac{\partial \mathbf{B}}{\partial t} \quad \Rightarrow \quad u = iR + L\frac{di}{dt} \tag{1}$$

$$\nabla \times \mathbf{H} = \mathbf{J} \quad \Rightarrow \quad \mathcal{F} = \phi\mathcal{R}(\phi) \tag{2}$$

where $\mathcal{F}$, $\mathcal{R}$, and ϕ represent magnetomotive force, magnetic reluctance, and magnetic flux, respectively. Equation (2) is the governing equation for magnetic equivalent circuit (MEC) modeling. For the device, the geometry can be substituted by an equivalent electric resistor circuit by means of (1) and (2). The electric circuit can be solved by applying Kirchhof's circuit laws yielding a system of equations. For (1) this yields good results, because the electric field focuses in the direction along the wires in the device. The paths of the wires in the device are well defined. For (2), however, this does not hold. The flux paths are not *a priori* known. First, a prediction of likely flux paths has to be made. By means of the estimated flux paths, secondly the magnetic reluctances, $\mathcal{R}$, can be determined. In the electrical steel of the device the determination of the flux paths is not troublesome, but in the air gap (where the field distribution is of most importance) the flux paths are very difficult to predict due to the

Digital Object Identifier 10.1109/TMAG.2007.914513

Color versions of one or more of the figures in this paper are available online at http://ieeexplore.ieee.org.

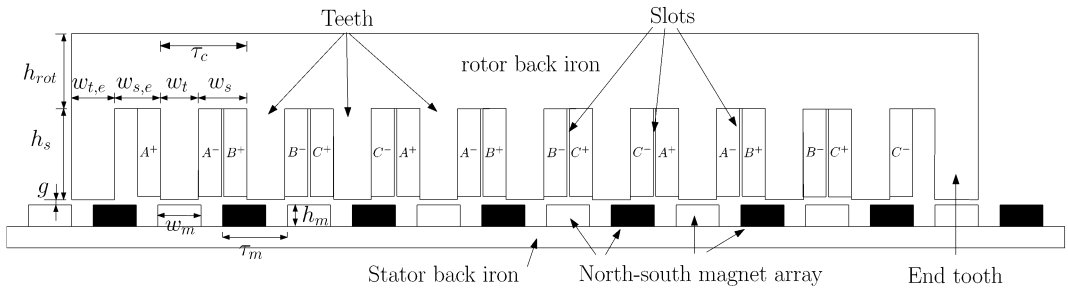

Fig. 1. Cross section of the three-phase PMSLM with some parameters. (All notations are specified in Table I of the Appendix.)

fringing and leaking of the flux. An additional complexity is incorporating a movement into the model. Then, the air-gap reluctances also become position dependent. The main advantages of this approach is the modeling of nonlinearities of the steel due to the dependency of $\mathcal{R}$ on ϕ and the low computational time. Also, the complexity of the geometry poses no problem for the MEC method. In principle, each element of the structure can be represented by reluctances. For a detailed field distribution in the air gap, this method is too coarse to acquire good results. The MEC method provides an estimate of the average flux in those parts of the geometry that are modeled as single reluctances. It gives no information on local flux distribution. An elaborate analysis of MEC modeling is given in [2].

Another way of determining the field in the air gap of the cross section of a PMLSM is based on the theory of vector magnetic potential, $\mathbf{A}$. The potential can be found by solving Poisson's equation in a 2-D domain

$$\nabla^2 \mathbf{A} = -\mu_0 J_z \tag{3}$$

and for source-free regions, Poisson's equation reduces to Laplace's equation

$$\nabla^2 \mathbf{A} = 0. \tag{4}$$

The equations can only be solved when the boundary conditions are known. The vector magnetic potential, $\mathbf{A}$, can only be solved analytically if the shapes of the boundaries are simple, e.g., annular, rectangular, or two infinitely long, infinitely deep parallel long plates. See [3]. For the structure of Fig. 1, $\mathbf{A}$ cannot be solved due to the complex slotted structure of the boundary. To acquire an approximate solution, the slotted structure could be neglected and regarded as a plate. A correction factor known as Carter's coefficient is then introduced. Carter's coefficient calculates the "effective" air-gap length for the slotless structure. For both the MEC and the analytical approach, Carter's coefficient can be introduced [4]–[6]. Analytical solutions for the newly obtained structure are readily available. Effects on the field due to slotting or nonperiodicity are not included. Also, the field distribution in the electric steel of the machine cannot be determined via this method. Thus, the application is restricted to linear cases only. Nevertheless, the magnetic field distribution is known for any point in the air gap.

The SC mapping allows the air-gap region in 2-D to be mapped through a mapping function to another one, less complex 2-D domain. This domain is called the canonical domain. The canonical domain can be of, e.g., rectangular or annular shape depending on the mapping function. The complete geometry of the air-gap region can be mapped to the canonical domain. In the canonical domain, (3) and (4) can now be solved analytically. Applying the mapping function to the solution for the vector potential $\mathbf{A}_c$ in the canonical domain enables one to find the vector potential $\mathbf{A}_o$ in the original air-gap domain. In this manner, an exact solution for each point in the original air-gap region can be determined for linear cases. The most complex part of the SC method is finding the mapping function. The freely available SC Toolbox for Matlab[1] is used to find the mapping function. Once the field distribution in the air gap is known, the force on the mover of the PMLSM can be determined in several ways. Determination of force by means of Lorentz's force formula cannot be done for slotted structures, because the formula does not take forces due to magnetization of the the electrical steel of the teeth into account. A general way of determining the force is the use of the Maxwell stress tensor (MST). The use of the MST requires the field to be known at every point along the closed surface. To find the force profile by means of MEC, the MST is thus not applicable, because MEC does not give field solutions for every point in the air gap. Instead, the principle of virtual force (VF) is used. This paper analyzes the same PMSLM via the two different approaches to show its discrepancies. First, the machine is analyzed by means of MEC modeling and then analyzed by means of solving the magnetic vector potential.

II. Field and Force Analysis Through MEC

A. Permeances in MEC Model

In linear cases, the reluctance of a flux tube is given by [2]

$$\mathcal{R} = \frac{1}{\mu_0 \mu_r} \int_L \frac{dl}{A(l)} \tag{5}$$

or expressed in permeances, $\mathcal{P}$

$$\mathcal{P} = \frac{1}{\mathcal{R}} \tag{6}$$

where l is the length of the flux tube in the direction of the flux and A is the area of the cross section of the flux tube perpendicular to the flux flow. The flux tubes in the rotor have the shape as depicted in Fig. 2. Reference [2] states that the position dependency of the air-gap permeance, including flux fringing, between the ith-tooth and jth-magnet can be represented as

$$\mathcal{P}_{ij} = g_{ij}(\Delta x)\mathcal{P}_{\max} \tag{7}$$

[1]http://www.math.udel.edu/~driscoll/SC/

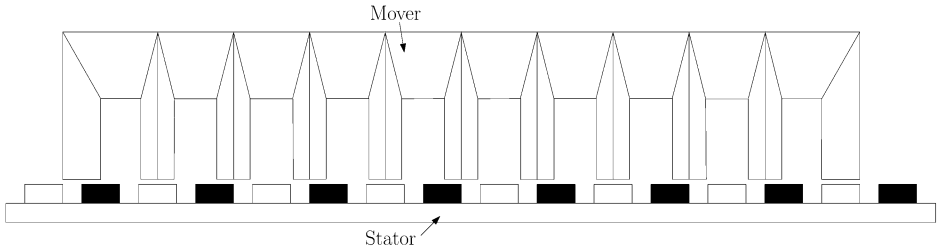

Fig. 2. Shapes of flux tubes of mover part of the PMLSM.

where

$$g_{ij}(\Delta x)=\begin{cases}1 & \Delta x<|Q_1|,\\ \frac{1}{2}+\frac{1}{2}\cos\left(\frac{\Delta x+K_{ij}-Q_1}{\tau_m-Q_1}\pi\right) & Q_1\le\Delta x\le Q_2,\\ \frac{1}{2}+\frac{1}{2}\cos\left(\frac{\Delta x+K_{ij}+Q_1}{\tau_m-Q_1}\pi\right) & Q_3\le\Delta x\le Q_4,\\ 0 & \text{elsewhere}\end{cases} \tag{8}$$

with

$$\begin{aligned}K_{ij}&=i\tau_c-j\tau_m,\\ Q_1&=\frac{1}{2}|w_m-w_t|-K_{ij},\\ Q_2&=\tau_m-K_{ij},\\ Q_3&=-\tau_m-K_{ij},\\ Q_4&=-\frac{1}{2}|w_m-w_t|-K_{ij}.\end{aligned}$$

$\mathcal{P}_{\max}$ is the air-gap permeance of the flux tube between an aligned tooth and magnet. There are also leakage flux paths present. These are implemented in the MEC model by means of extra permeances. The permeances in the back iron are much higher than the the permeance of the magnets. Therefore, the back iron permeances are assumed to be infinite in the model for simplicity.

B. Equivalent Sources of Magnetic Flux

The sources of magnetic flux are the coils in the system and the permanent magnets. Their equivalent voltage sources need to be expressed by means of magnetomotive force (MMF). For the coils, the position-dependent MMF is equal to

$$\mathcal{F}_{a,b,c}=Ni_{a,b,c}(x) \tag{9}$$

where the subscripts indicate the phases. The MMF source for the magnets is equivalent to

$$\mathcal{F}_m=-H_ch_m \tag{10}$$

where H_c is the coercivity of the permanent magnets.

C. Equivalent Circuit

The equivalent electric circuit is shown in Fig. 3. Between each tooth (indicated by the upper numbers) and magnet (indicated by the lower numbers), position-dependent permeance $\mathcal{P}_{ij}$ is placed. Subscripts i and j represent the tooth number and magnet number, respectively. The alternately North–South (NS) magnet array is modeled as being periodical as can be seen from the leakage permeance between magnets 1 and 18 in Fig. 3. This is done to model the magnet array as infinitely long. This is a valid assumption since in practice the stator part is much longer than the mover part. The admittance matrix, $\mathbf{G}$, and source vector, $\mathbf{\Phi}$, can now be found by applying Kirchoff's current law for each node in the schematic of Fig. 3. Now, the MMF vector, $\mathbf{F}$, of the nodes can be determined.

D. Force Calculations

The force profile can only be calculated by means of virtual force method. In order to find the force profile the total energy or co-energy in the air gap and magnets need to be known. In linear cases, energy and coenergy are the same. The energy in the air gap can be found by adding the energy in each permeance in the air gap and magnets [7], [8]

$$E_{\text{gap}}=\frac{1}{2}\sum_i\sum_j\mathcal{F}_{ij}^2\mathcal{P}_{ij}+\frac{1}{2}\mathcal{P}_{pm}\sum_k\mathcal{F}_k^2. \tag{11}$$

$\mathcal{F}_{ij}$ is the MMF drop over $\mathcal{P}_{ij}$ and $\mathcal{F}_k$ is the MMF drop over $\mathcal{P}_m$ of the kth magnet. The energy difference between two subsequent positions is equal to the work done by the system. The thrust force on the mover relates to the work as

$$F=-\left.\frac{dW}{dx}\right|_{i=\text{const.}} \tag{12}$$

To find the force as a function of displacement, $\mathcal{P}_{ij}$ and MMF need to be recalculated first. The new values then need to be assigned to the accompanying elements in Fig. 3. For each position, the matrices describing the schematic of Fig. 3 need to be solved again. It is important to notice that in (12) the currents in the system need to be constant, however, the currents vary as the position varies. To obtain correct results for each position, the energy is determined for two very close points around that position, while keeping the current fixed. The results presented in Fig. 4 are obtained for the force profile of the PMLSM.

III. Schwarz-Christoffel Mapping

The SC theorem [9] states that the interior respectively exterior of any polygon can be mapped to the upper respectively lower complex half-plain by a complex function $f(z)$:

Let P be the interior of a polygon Γ having vertices $w_1,\ldots,w_n$ and interior angles $a_1\pi,\ldots,a_n\pi$ in counterclockwise order. Let f be any conformal map from the upper half-plane H^+ to P with $f(\infty)=w_n$. Then, for some complex constant A and C, where $w_k=f(z_k)$ for $k=1,\ldots,n-1$

$$f(z)=A+C\int_{z_0}^{z}\prod_{k=1}^{n-1}(\zeta-z_k)^{a_k-1}d\zeta. \tag{13}$$

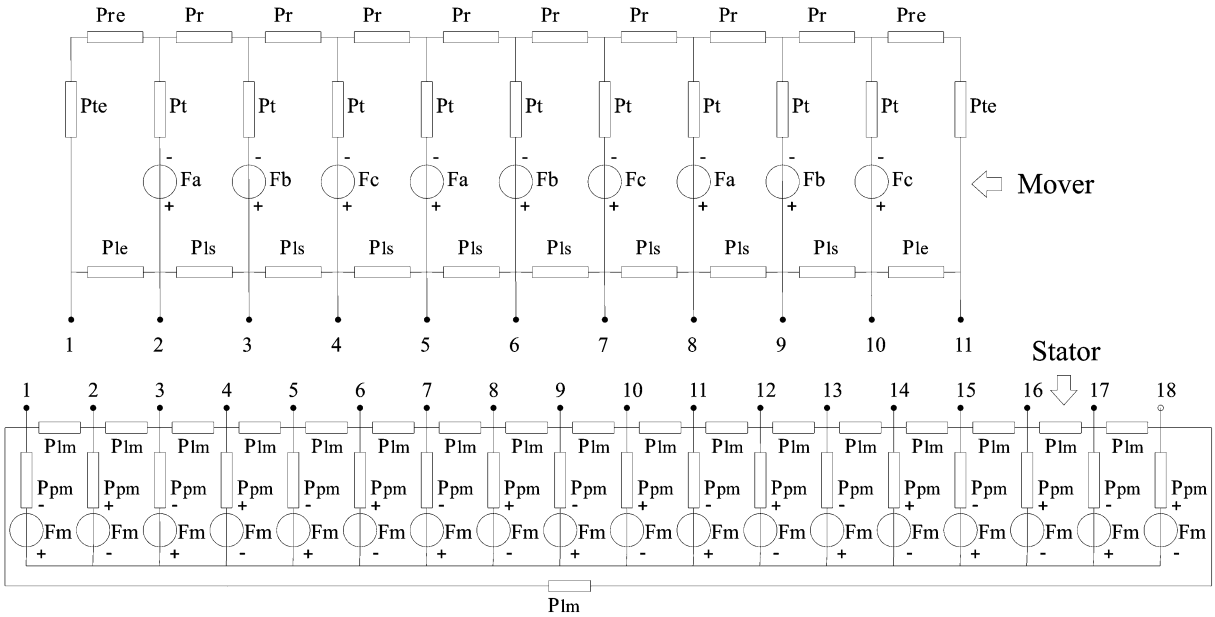

Fig. 3. Equivalent electric circuit of the PMLSM of Fig. 3.

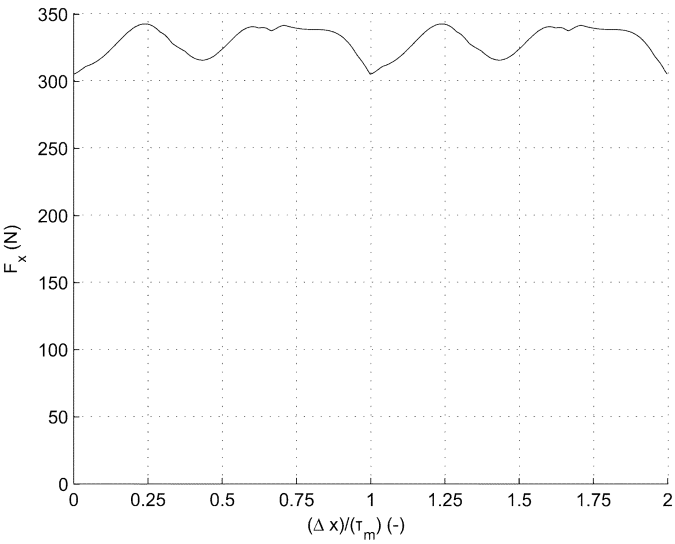

Fig. 4. Force profile of the PMLSM obtained by MEC modeling.

The right angles between flux lines and equipotential lines are preserved under the mapping $f(z)$. Thus, potential functions under $f(z)$ are invariant. Expression (13) can be manipulated in such a way that the interior of the polygon can be mapped to a rectangular canonical domain instead of the upper complex half-plane. The values for A, C, and the points z_k cannot be determined analytically when the polygon contains more then three vertices. The SC toolbox solves A, C, and z_k numerically with very high precision. In the SC toolbox, other features are implemented that are useful for SC mapping. It is not the goal of this paper to give a profound analysis of the SC mapping theory, but rather to show the usefulness of its application in electromechanics. More information on the theory of SC mapping and the use of SC toolbox can be found in [10]–[14].

IV. SC Method

The same PMLSM as depicted in Fig. 1 will now be analyzed using the SC method. A lot of the presented work here is based on [15]. The back iron and the mover iron consist of linear iron with permeability $\mu_r = 10^3$. The analysis also holds for nonlinear materials as long as the machine is not operating in the saturated region of the B–H curve of the material. The coordinates of the vertices of the polygon formed by the shape of the air gap need to be expressed in a complex number w, where the real part equals the x-component and the imaginary part equals the y-component. So, for the kth vertex w_k follows:

$$w_k(x_k, y_k) = x_k + y_k j. \tag{14}$$

To take end effects into consideration, the air-gap region at both end teeth is expanded in a manner as depicted in Fig. 5. Fig. 5 represents the air-gap region in the complex w-plane. The height of the expanded air-gap region is chosen to be $h_{\mathrm{g,ex}} = h_m + g + 3h_s$ (see Fig. 1) and the width is set to $w_{g,ex} = 3\tau_m$. Furthermore, the rectangular conductors in the slots of the machine are reduced to line conductors. Each magnet is modeled as two current sheets along the sides of the magnet. Thereafter, all sheets are represented by a number of line currents. In this way, the air gap now only contains line currents as can be seen in Fig. 5. These assumptions have ultimately no disturbing effect on the field distribution in the gap and save computation time. To map the slotted structure to the rectangular complex z-domain, $f(z)$ has to be calculated. This is done by using the "crrectmap" statement in the SC toolbox. The vertices in Fig. 5 indicated with □-mark are assigned to be the corner points of the rectangular domain. Once $f(z)$ is known, the positions of the conductors in the mapped domain can also be found by using the SC toolbox. The resulting mapped geometry in the z-domain is represented in Fig. 6.

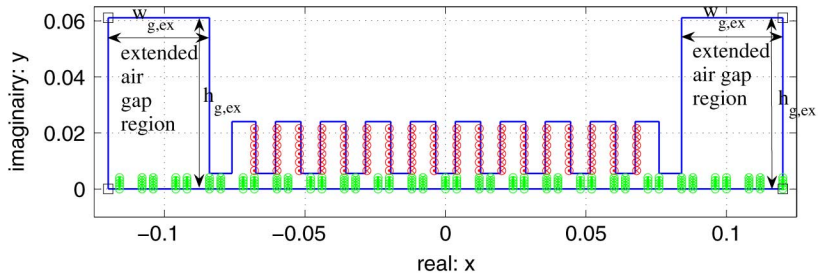

Fig. 5. Representation of the slotted structure and position of conductors in the complex w-plane.

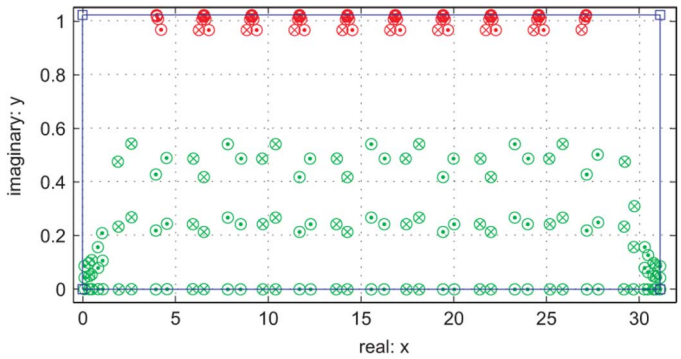

Fig. 6. Representation of the mapping of the slotted structure and position of conductors in the complex z-plane.

A. Field Calculations

Before the field distribution due to the line currents can be calculated in the z-domain, the boundary conditions at the edges of the rectangle have to be determined. Both the back iron and the mover iron consist of linear soft magnetic material with $\mu_r \gg \mu_0$. The soft magnetic material can be assumed to be infinitely permeable. Thus, for the top and bottom edges of the rectangle the boundary conditions apply for which the tangential component of the $\mathbf{B}$ field is absent. The magnets past the left and right edges of the rectangle contribute to the force component due to the end effects. Therefore, the field distribution near the end tooth as a consequence of these magnets has to be taken into consideration as well. For this purpose, the extended air-gap regions are introduced for the left and right ends of the model. In the w-domain, however, there is no iron above the magnets past the end teeth outside the real air gap. To minimize the effect of the iron in the w-domain on the field distribution past the end teeth, the extended air-gap height is set to $h_{g,ex} \gg g+h_m+h_s$. There are no restrictions on the left and right side boundaries. The slotted model is now reduced to a problem for magnetic field distribution between two infinitely long, infinitely permeable parallel plates. When nonlinear materials are used for the back iron and mover iron, this assumption is still valid as long as the material is not saturated. The values of the line currents of the coils are as given in (9) except that they are divided into line currents. So, the value per line current given by (9) is divided by the number of line currents per phase. A magnetized body can be substituted by equivalent currents via the relationships

$$\mathbf{J} = \nabla \times \mathbf{M} \tag{15}$$

$$\mathbf{J}_s = \mathbf{M} \times \mathbf{n}. \tag{16}$$

The magnetization of the magnets is in either the positive or negative y-direction. Therefore, in (15) the volume current density becomes $\mathbf{J} = 0$. The surface current density in (16) becomes $\mathbf{J}_s = \pm M\hat{\mathbf{z}}$ and flows in the lateral side of the magnets only. Since the sheet currents are reduced to line currents, the total expression for line currents is expressed as

$$I_m = -\frac{Mh_m}{k_m} \tag{17}$$

where k_m is the number of line currents a current sheet is divided by. In advance, it is not known where the operation point on the demagnetization curve of the magnets is. To minimize the error, a halfway point at the demagnetization curve is chosen as operating point. M in (17) becomes [16]

$$M = \frac{B_r}{\mu_0} + \frac{Hc}{2}(\mu_{pm} - 1) \tag{18}$$

where Br is the remanence of the magnets. Effects caused by mover displacement can be incorporated into the model by translating the position of the line currents due to the magnets relative to the line currents due to the conductors in the z-domain. The position of the line currents of the magnets in the w-domain becomes a function of displacement

$$w_{k,pm}(\Delta x) = w^0_{k,pm} - \Delta x \tag{19}$$

where $w^0_{k,pm}$ is the initial position of the line currents when $\Delta x = 0$. The new positions are then mapped to the z-domain using (13). To implement the movement correctly, care is to be taken when the position of the sheet currents of the magnets translates beyond the rectangular domain. Each current sheet leaving the rectangle through one edge has to enter through the opposite edge. Furthermore, when currents sheets belonging to the same magnets become separated by the boundary edge of a domain, an additional current sheet positioned at the boundary edge has to be added to guarantee proper field solutions. When the value of the currents and the position of the nth-line current is allocated correctly, the field solution for the components of the flux density due to the nth-line current at position $z = u+vj$ in the z-domain between two infinitely long, infinitely permeable plates follows [3]:

$$B^n_u(z) = \frac{I_n\mu_0}{4l}\left[\frac{\sin\frac{\pi}{l}(v+h)}{\cosh\frac{\pi}{l}u - \cos\frac{\pi}{l}(v+h)} + \frac{\sin\frac{\pi}{l}(v-h)}{\cosh\frac{\pi}{l}u - \cos\frac{\pi}{l}(v-h)}\right], \tag{20}$$

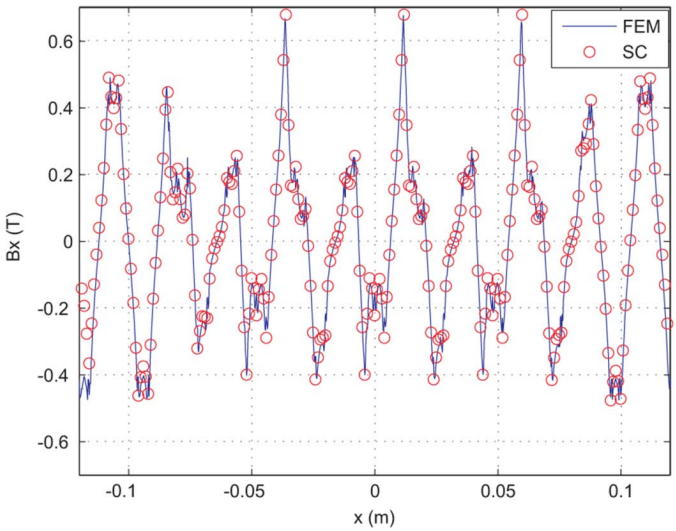

Fig. 7. Comparison of the SC with the FEM for the x-component of the flux density along a line halfway through the air gap and $\Delta x = 0$.

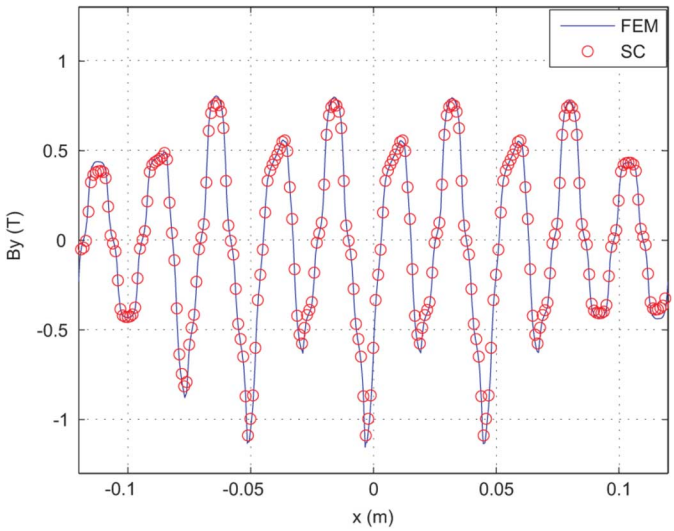

Fig. 8. Comparison of the SC with the FEM for the y-component of the flux density along a line halfway through the air gap and $\Delta x = 0$.

$$B_v^n(z) = -\frac{I_n \mu_0}{4l}\left[\frac{\sinh\frac{\pi}{l}u}{\cosh\frac{\pi}{l}u - \cos\frac{\pi}{l}(v+h)} + \frac{\sinh\frac{\pi}{l}u}{\cosh\frac{\pi}{l}u - \cos\frac{\pi}{l}(v-h)}\right] \tag{21}$$

where l is the distance between the plates, and h is the distance between the line current and the lower plate. To find the complex flux density due to all line currents at z, the next approach is applied:

$$B(z) = \sum_{n=1}^{V} B_u^n(z) + B_v^n(z)j \tag{22}$$

where V is the total number of line currents in the model. For each position, the complex flux density in the rectangular domain is known. Although the complex potential function of the field is invariant under $f(z)$, the flux density, however, is not, because the solution is determined by a system dependent gradient. Therefore, a transformation, given by [11], has to be applied to the solution in the z-domain to obtain the solution in the original w-domain:

$$B(w) = \frac{B(z)}{\overline{f'(z)}} \tag{23}$$

where $\overline{f'(z)}$ is the complex conjugate of the derivative of the map, which can also be computed with a statement in the SC toolbox. Finally, the field distribution along a line in the air gap of the slotted machine can be determined. Figs. 7 and 8 show the results for the flux density components B_x, and B_y, respectively, along a halfway line across the air gap compared to the FEM results. The FEM results are obtained by using the Cedrat FLUX 2D package, version 9.3.2. The graphs show that the results of the SC method for magnetic fields match the results obtained by FEM with very high precision.

B. Force Calculations

With the known flux density distribution in the air gap, the force profile of the PMSLM can be determined. The force is calculated by means of the Maxwell stress tensor in 2-D [1], because the magnetic field distribution is known for each point in the air gap. The force could also be calculated by means of using virtual force method. This method requires the field to be known over the entire air gap instead of a line (in the case for MST). This would significantly increase calculation time. To be able to calculate the force profile a closed path, along which the MST is to be integrated, is chosen as depicted in Fig. 9. Because path $L3$ in Fig. 9 is in the high permeable iron, it has no significant contribution to the force distribution and therefore can be excluded from the calculation. The expression for the force in the direction of movement now becomes

$$F_x = \frac{d}{\mu_0}\left[\int_{L1} B_x B_y dx + \int_{L2} \frac{B_x^2 - B_y^2}{2} dy + \int_{L4} \frac{B_y^2 - B_x^2}{2} dy\right] \tag{24}$$

where d is the depth in [m] of the PMLSM. It appears that the integrals over the paths $L2$ and $L4$ (Fig. 9) in (24) do not contribute significantly to the force profile. These expressions can thus also be removed from (24) to save computation time. The remaining expression is evaluated numerically. If one is also interested in the normal force component, it can be calculated in a similar way applying the Maxwell stress tensor. The results compared to the FEM results, for a current with an amplitude of 8A, are depicted in Fig. 10 and a zoomed image of the force profile compared to the FEM is presented in Fig. 11. Figs. 10 and 11 show that the SC method gives much more accurate results for the shape of the force profile, caused by end effects and cogging force due to the finite, slotted structure of the actuator and acceptable results for average total force, than the MEC model. The error for average force between the SC and the FEM results is 1.2% and the error between MEC and FEM solutions for the average force is 6.6%. The MEC model does not provide perfect result for the force profile. Furthermore, the peaks are much higher relative to the average value of the force compared to SC and FEM results. Additionally, the SC results are compared with results from FEM under saturated conditions of

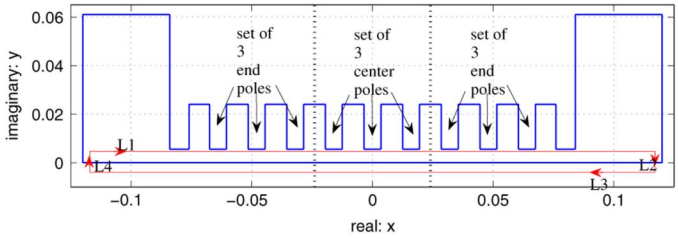

Fig. 9. Closed path along which the Maxwell stress tensor is calculated in the w-domain.

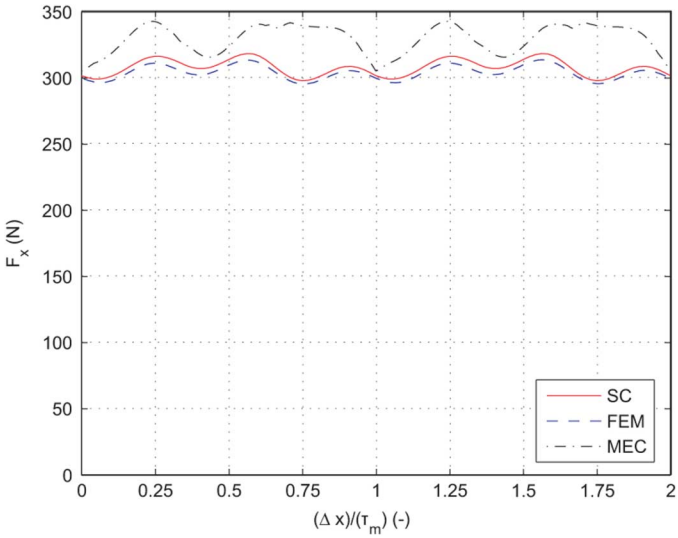

Fig. 10. Comparison of the thrust force obtained by the MEC, the SC, and the FEM as a function of displacement.

the nonlinear rotor iron. Fig. 12 shows the results for currents with amplitudes of 8A, 12A, and 16A. Fig. 12 shows that the SC method provides accurate results for machines operating under not too heavily saturated conditions. It can be concluded that the SC method is a much more accurate design tool than MEC modeling. Explanation for the difference between SC and FEM, is the way of modeling the permanent magnets and the manner in which the currents are determined by (17) and (18). This approximation does not take the actual working point on the demagnetization curve of the magnets into consideration. Better results could possibly be obtained by modeling the magnets by means of magnetic charges, but such an approach has to be examined in further research. Nevertheless, the presented SC method allows for an accurate analysis of the cogging component and end effect component present in the total force profile as well as a good approximation for the average total force. If the machine contains more sets of three center poles instead of one set of three center poles in between the two sets of end poles (Fig. 9), additional vertices to the polygon in the w-domain do not necessarily have to be added to acquire an accurate force profile. Because of the periodicity of the structure of the PMSLM for all set of three mover poles (center poles) in between the two sets of three mover poles at the ends of the mover, the field distribution in the air gap is repetitive for each set of three mover poles in between the six end poles (Fig. 9). Here, the end teeth are not regarded as poles because they are not magnetized by

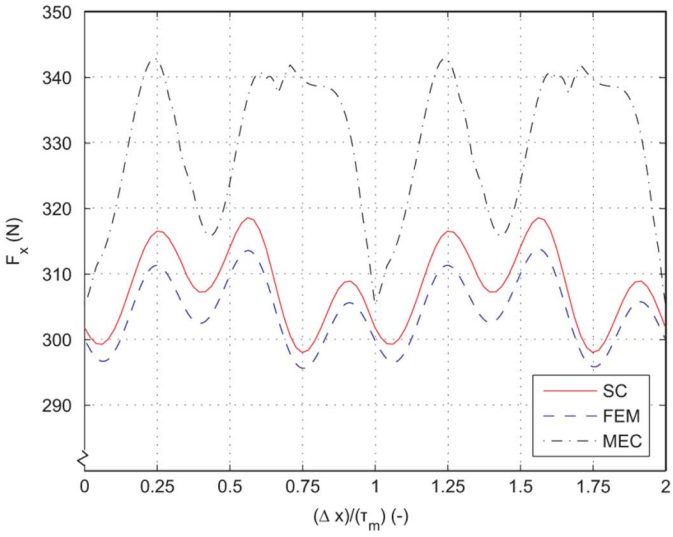

Fig. 11. Close up look of the comparison of the thrust force obtained by the MEC, the SC and the FEM as a function of displacement.

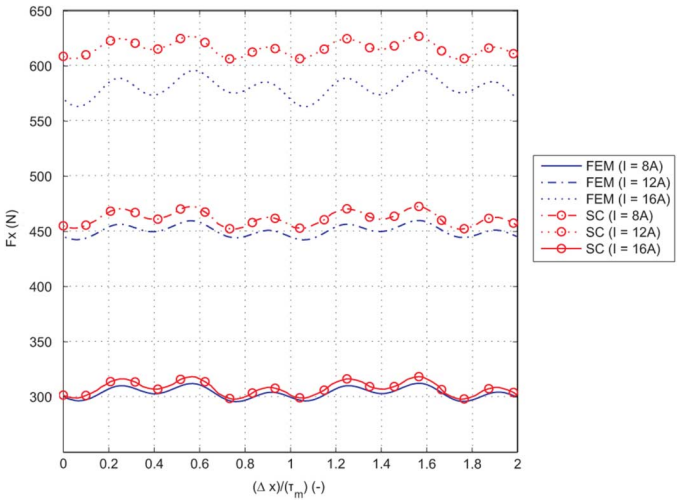

Fig. 12. Force profile acquired by the SC method compared with FEM results under saturated conditions.

coils. This is visualized in Fig. 9. The same polygon can thus be applied, only the portion of the force due to the part of path $L1$ directly under the center poles needs to be multiplied by the total number of center poles in the PMLSM. A lot of extra computation time can be saved in this way.

V. Conclusion

A simple approach to implement a tool to analyze, design or optimize a nonsaturated PMLSM has been presented in this paper. The accuracy of the SC method for both field distribution in the air gap and force profile has been justified by comparison with results acquired from the FEM 2-D software. The SC method presented in the paper, however, gives no information about the field distribution in the iron of the machine. Then, the SC method may not be of much use in cases where eddy currents have a significant influence on the field distribution and the performance of the PMLSM. The amount of the computational

TABLE I
ADDITIONAL GEOMETRIC PARAMETERS OF THE PMLSM

parameter	value (mm)
g	1.5
h_m	4
w_m	8
τ_m	12
τ_c	16
w_t	7
w_s	9
$w_{t,e}$	8
$w_{s,e}$	8.5
h_s	18.5
h_{rot}	14.75

TABLE II
ADDITIONAL PHYSICAL QUANTITIES OF THE PMLSM

parameter	value
N	125
B_r	1.23 T
H_c	$8.9.10^5$ A/m
μ_{pm}	1.09

time used by the SC method is highly dependent on the number of line currents used in the model and is also much longer than the computational time for obtaining the force profile by means of the MEC. The inverse mapping of the line currents from the w- to z-domain occupies about 65% of the total computational time. Total computational time is thus highly dependent on the required accuracy. Still, the SC method is faster then FEM and allows for easier change of machine parameters in order to be optimized. It is shown that the SC method is potentially a very suitable design tool. For the wide class of long-stroke and short-stroke iron and ironless linear machines, a combination of the MEC and SC method is probably the fastest way of designing a PMLSM. The MEC can be used for a rough estimate design and SC can be used for fine tuning the design.

APPENDIX
PARAMETERS OF THE PMLSM

Additional geometric parameters presented in Fig. 1 of the PMLSM are given in Table I and physical quantities are listed in Table II.

ACKNOWLEDGMENT

The authors would like to thank Dr. A.P.J. van Deursen for his help on gaining insight on conformal mapping and the use of the Schwarz-Christoffel toolbox.

REFERENCES

[1] E. P. Furlani, *Permanent Magnet and Electomechanical Devices*. New York: Academic, 2001.
[2] V. Ostovic, *Dynamics of Saturated Electric Machines*. Berlin, Germany: Springer-Verlag, 1989.
[3] B. Hague, *Electromagnetic Problems in Electrical Engineering*. London, U.K.: Oxford Univ. Press, 1929.
[4] J. Wang, G. W. Jewell, and D. Howe, "A general framework for the analysis and design of tubular linear permanent magnet machines," *IEEE Trans. Magn.*, vol. 35, no. 3, pp. 1986–2000, May 1999.
[5] G. Xiong and S. A. Nasar, "Analysis of fields and forces in a permanent magnet linear synchronous machine based on the concept of magnetic charge," *IEEE Trans. Magn.*, vol. 25, no. 3, pp. 2713–2719, May. 1989.
[6] H. Polinder, J. G. Slootweg, M. J. Hoeijmakers, and J. C. Compter, "Modeling of a linear PM machine including magnetic saturation and end effects: Maximum force-to-current ratio," *IEEE Trans. Ind. Appl.*, vol. 39, no. 6, pp. 1681–1688, Nov. 2003.
[7] D. C. Hanselman, *Brushless Permanent Magnet Motor Design*. London, U.K.: McGraw-Hill, 1994.
[8] A. E. Fitzgerald, C. Kingsley, Jr., and S. D. Umans, *Electric Machinery*. London, U.K.: McGraw-Hill, 2003.
[9] T. A. Driscoll and L. N. Trefethen, *Schwarz-Christoffel Mapping*. Cambridge, U.K.: Cambridge Univ. Press, 2002.
[10] T. A. Driscoll, *Schwarz-Christoffel Toolbox User's Guide: Version 2.3*. Newark, DE: Dept. Math. Sci., Univ. Delaware, 2005.
[11] P. Henrici, *Applied and Computational Complex Analysis Volume 3: Discrete Fourier Analysis, Cauchy Integrals, Construction of Conformal Maps, Univalent Functions*. New York: Wiley, 1986.
[12] K. J. Binns, P. J. Lawrenson, and C. W. Trowbridge, *The Analytical and Numerical Solution of Electric and Magnetic Fields*. New York: Wiley, 1992.
[13] V. I. Ivanov and M. K. Trubetskov, *Handbook of Conformal Mapping with Computer-Aided Visualization*. London, U.K.: CRC, 1994.
[14] L. V. Bewley, *Two-Dimensional Fields in Electrical Engineering*. New York: Dover, 1963.
[15] T. C. O'Connell and P. T. Krein, "A preliminary investigation of computer-aided Schwarz-Christoffel transformation for electric design and analysis," presented at the IEEE Workshops Comput. Power Electron., 2006.
[16] M. Markovic, M. Jufer, and Y. Perriard, "Reducing the cogging torque in brushless DC motors by using conformal mappings," *IEEE Trans. Magn.*, vol. 40, no. 2, pp. 451–455, Mar. 2004.

Manuscript received July 30, 2007; revised December 7, 2007. Corresponding author: D. C. J. Krop (e-mail: d.c.j.krop@tue.nl).